N86-27206

Thomas A. Buter and Donald P. Rizzetta
Air Force Wright Aeronautical Laboratories
Wright-Patterson Air Force Base, Ohio

ABSTRACT

Steady solutions about a slender sharp-edged delta wing in a supersonic freestream for moderate and high angles of attack are obtained numerically by time integration of the unsteady compressible three-dimensional laminar Navier-Stokes equations. The main features of the flow, including primary and secondary separation, and vortex position and strength, are adequately simulated in the numerical solutions. Improved resolution of the computational grid in the leading-edge region from a previous solution had considerable effect on the accuracy of the solutions. Good agreement between numerical solutions and experimental data was obtained for two cases. A local timestepping procedure is used to speed convergence by approximately a factor of two.

NOMENCLATURE

A	attachment line
c	speed of sound $(\gamma RT)^{\frac{1}{2}}$
C_p	pressure coefficient, $2(P-P_\infty)/\rho U_\infty^2$
e	internal specific energy
E	total specific energy
F,G,H	vector fluxes
L	model length, mm
M	freestream Mach number
P	pressure
Pr	Prandtl number, 0.73 for air
q_x, q_y, q_z	components of heat flux vector
R	gas constant
Re	Reynolds number, based on the root chord
S	separation line
t	time
T	temperature
u,v,w	Cartesian velocity components in x,y,z directions, respectively
$u_{1,2,3}$	u,v,w
U	vector of mass averaged variables
x,y,z	Cartesian coordinates in axial, normal, and spanwise directions, respectively
α	angle of attack
β	numerical damping coefficient
γ	ratio of specific heats
Δ	finite difference step size

μ	molecular viscosity coefficient
ε, η, ζ	transformed body fitted coordinates
ρ	density
$\tau_{xx}, \tau_{xy}, \tau_{xz},$ $\tau_{yy}, \tau_{yz}, \tau_{zz}$	components of viscous stress tensor

Subscripts

aw	adiabatic wall value
LE	evaluated at wing leading edge
max	maximum value
min	minimum value
loc	local value
T	pitot conditions
∞	freestream value

INTRODUCTION

In recent years, with the advent of the supercomputer, computational aerodynamicists have devoted considerable effort to the solution of increasingly complex three-dimensional separated flows with a view toward the solution of airframe design problems. One of the most interesting and most practical of these is the separated flow field associated with a slender sharp-edged delta wing at angle of attack. Characterized by a pair of leeward spiraling vortices emanating from the separated leading-edge flow this inviscid-viscous flow problem has been computed using several techniques. Higher order panel methods (1-3) have enjoyed some measure of success by modeling the vortex roll-up as a sheet of quadratic doublets. However, this method requires the presence of a vortex and some awareness of its size and position. These restrictions are removed when a 3-D Euler approach is used (4,5). The physical meaning of such solutions is questionable, however, given the apparent dependency on grid resolution (6) and on the use of numerical viscosity. Using a conical flow approximation, Vigneron (7) et al. obtained a Navier-Stokes solution for a delta wing having a subsonic leading edge. With this approach, the location and basic structure of the primary vortex may be accurately computed. However, in cases where the adverse pressure gradient in the outboard region of the wing, induced by the leading-edge expansion, is of sufficient strength to produce a secondary separation, the conical approach becomes inadequate as evidenced by the results of Reference 7. Previous results presented by Rizzetta and Shang (8) illustrated that by using the full 3-D compressible laminar Navier-Stokes equations secondary effects may be accurately resolved numerically. The current investigation adopts this technique for an additional high angle-of-attack case and attempts to enhance the results of the previous study by improving the grid resolution and leading-edge definition. The present study investigates numerically the 75° sweep delta wing studied experimentally by Monnerie and Werle (9) depicted in Figure 1.

The governing equations for this computation are taken to be the unsteady compressible three-dimensional Navier-Stokes equations in mass-averaged variables which may be expressed notationally in the following chain-rule conservative form:

$$\frac{\partial U}{\partial t} + (\frac{\partial \xi}{\partial x}, \frac{\partial \xi}{\partial y}, \frac{\partial \xi}{\partial z}) \begin{bmatrix} \frac{\partial F}{\partial \xi} \\ \frac{\partial G}{\partial \xi} \\ \frac{\partial H}{\partial \xi} \end{bmatrix} + (\frac{\partial \eta}{\partial x}, \frac{\partial \eta}{\partial y}, \frac{\partial \eta}{\partial z}) \begin{bmatrix} \frac{\partial F}{\partial \eta} \\ \frac{\partial G}{\partial \eta} \\ \frac{\partial H}{\partial \eta} \end{bmatrix} + (\frac{\partial \zeta}{\partial x}, \frac{\partial \zeta}{\partial y}, \frac{\partial \zeta}{\partial z}) \begin{bmatrix} \frac{\partial F}{\partial \zeta} \\ \frac{\partial G}{\partial \zeta} \\ \frac{\partial H}{\partial \zeta} \end{bmatrix} = 0 \quad (1)$$

Here x,y,z are Cartesian coordinates in the axial, normal and spanwise directions respectively and ϵ,η,ζ are the corresponding transformed coordinates in a body-oriented system and

$$U = \begin{bmatrix} \rho \\ \rho u \\ \rho v \\ \rho w \\ \rho E \end{bmatrix} \quad (2)$$

$$F = \begin{bmatrix} \rho u \\ \rho u^2 + \tau_{xx} \\ \rho uv + \tau_{xy} \\ \rho uw + \tau_{xz} \\ (\rho E + \tau_{xx}) u + \tau_{xy} v + \tau_{xz} w - q_x \end{bmatrix} \quad (3)$$

$$G = \begin{bmatrix} \rho v \\ \rho v u + \tau_{xy} \\ \rho v^2 + \tau_{yy} \\ \rho v w + \tau_{yz} \\ (\rho E + \tau_{yy}) v + \tau_{yx} u + \tau_{yz} w - q_y \end{bmatrix} \tag{4}$$

$$H = \begin{bmatrix} \rho w \\ \rho w u + \tau_{zx} \\ \rho w v + \tau_{zy} \\ \rho w^2 + \tau_{zz} \\ (\rho E + \tau_{zz}) w + \tau_{zx} u + \tau_{zy} v - q_z \end{bmatrix} \tag{5}$$

$$\tau_{xy} = \tau_{yx} = -\mu \left(\frac{\partial u}{\partial y} + \frac{\partial v}{\partial x} \right) \tag{6}$$

$$\tau_{xz} = \tau_{zx} = -\mu \left(\frac{\partial u}{\partial z} + \frac{\partial w}{\partial x} \right) \tag{7}$$

$$\tau_{yz} = \tau_{zy} = -\mu \left(\frac{\partial v}{\partial z} + \frac{\partial w}{\partial y} \right) \tag{8}$$

$$q_x = \frac{\mu \gamma}{Pr} \left(\frac{\partial e}{\partial x} \right) \tag{9}$$

$$q_y = \frac{\mu \gamma}{Pr} \left(\frac{\partial e}{\partial y} \right) \tag{10}$$

$$q_z = \frac{\mu \gamma}{Pr} \left(\frac{\partial e}{\partial z} \right) \tag{11}$$

$$E = e + (u^2 + v^2 + w^2)/2 \tag{12}$$

The Cartesian velocity components are given by u, v and w, ρ is the density, E the total energy per unit mass, and e the specific internal energy. Completion of this system is provided by the perfect gas law:

$$P = \rho R T \tag{13}$$

and the Sutherland law for the molecular viscosity coefficient μ. Freestream values are specified as boundary conditions for all dependent variables at the upstream, outboard, upper and lower computational boundaries, i.e., $U = U_\infty$. At the wing midspan a plane of symmetry is imposed which results in:

$$\frac{\partial \rho}{\partial \zeta} = \frac{\partial \rho u}{\partial \zeta} = \frac{\partial \rho v}{\partial \zeta} = \frac{\partial \rho E}{\partial \zeta} = w = 0 \text{ along } \zeta = 0 \tag{14}$$

On the upper and lower wing surface

$$u = v = w = 0$$
$$T = T_{aw}$$
$$\frac{\partial P}{\partial \hat{n}} = 0, \text{ where } \hat{n} \text{ is the unit normal to the surface} \tag{15}$$

Because only computations corresponding to supersonic freestream conditions were considered, no formal mathematical downstream boundary conditions were needed. However, due to the requirements of the numerical algorithm used, values of the dependent variables at the downstream computational boundary are obtained by second-order extrapolation from the interior domain.

The laminar computation performed in Reference 8 for M=1.95 and α=10° was repeated in the present study. Since it was of interest to compute a high angle of attack, a 20° case was chosen for the same Mach number. This necessitated increasing the size of the computational domain due to the expansion of the physical region of interest. The grid size was increased from 20 x 64 x 40 to 21 x 70 x 50 in the ξ,η,ζ directions and was algebraically generated in a fashion similar (Figure 2) with two notable exceptions. In the work of Reference 8 the plane of symmetry was straddled to obtain a second-order centered difference implementation of the symmetry condition. While this technique was successful, the grid in this region was rather coarse. For the present study points were exponentially clustered near the plane of symmetry (Figure 2) to improve resolution in that region. This becomes particularly critical for the 20° case because the gradients near the plane of symmetry are greater due to the growth of the primary vortex and its inboard migration. The second modification to the grid structure was made at the wing tip, where resolution was increased and hence it was expected that the expansion about the leading edge might be more accurately resolved. This improvement, however, was gained at the expense of decreasing the time step (Table 1) due to the decreased step size in the y direction. In order to alleviate some of this degradation of efficiency, the lower surface η lines were bent down and away from the surface near the tip, thereby increasing the size of Δy_{min} (Figure 3).

For the purpose of improved vortex resolution the current grid system employs an additional 6 η-grid lines (yielding a total of 46) on and above the wing surface and an additional 5 ζ-grid lines (total - 29) inboard of the wing leading edge. Further, 5 ζ-grid lines were added to the outboard field region to resolve the expansion about the leading edge. An additional η-ζ plane was added at $\frac{X}{L}$ = 0.05 to improve the resolution near the apex.

This grid, although sized for the α=20° case, was used for both the α=10° and 20° cases to determine if for the present α=10° case a higher degree of accuracy might be obtained than its predecessor and for the purpose of uniformity between the current solutions.

Steady-state solutions to Equation 1 were generated using the time-dependent explicit unsplit two-step predictor-corrector finite-difference algorithm due to MacCormack (10) which has evolved as a reliable technique for numerical solution of a wide variety of fluid dynamic problems. As part of this algorithm, a commonly employed fourth-order pressure damping term (11) was used to suppress numerical oscillations in regions with large gradients in the dependent variables. The form of this term is given as

$$\beta \, \Delta t \sum_{j=1}^{3} (\Delta v_j)^3 \frac{\partial}{\partial v_j} \left[\frac{\partial U}{\partial v_j} \left| \frac{\partial^2 P}{\partial v_j^2} \right| \frac{|u_j + c|}{P} \right] \text{ where } v_{1,2,3} = \xi, \eta, \zeta \tag{16}$$

which is then added to the new value of U at each time step. In the present study, as in the previous effort, a damping coefficient of β = 2.0 was used.

Freestream values were used as the initial conditions save for the interior boundary where surface conditions were applied. In order to remove the initial transients, the numerical flow fields were allowed to evolve for 100 time steps in the time accurate mode with Δt chosen such that the maximum Courant Fredicks Lewy (CFL) number was 0.5. Subsequently, the CFL number was increased to 0.8 and the computation was allowed to progress to steady state in a local timestepping fashion, where each grid point advances at its own rate (Δt_{loc} corresponding to a CFL number of 0.8) for a given iteration. This procedure has the advantage of advancing the solution to a steady-state value much more expeditiously since the more coarse regions of the physical domain are able to advance more quickly than in a time accurate mode. This modification resulted in the appearance of the primary and secondary vortex structures in the numerical solution much earlier than in the work of reference 8.

The computations were made on a Cray 1-S computer using a vectorized solver (12) written specifically for the Cray 1 computer. The solver advances the solution from one time step to the next in η-ζ planes by marching in the ξ-direction, thus minimizing the data flow to and from central memory. Using the previously defined computational grid, approximately 1.124×10^6 decimal words of storage were required. A data processing rate of 6.9×10^{-5} CPU seconds per time step per grid point was achieved where vectorization occurred in the ζ-direction, with a vector length of 50.

RESULTS

Numerical solutions were generated for the flow about the delta wing illustrated in Figure 1 at a Mach number of 1.95 (0.5 normal to the leading edge) for 10° and 20° angles of attack. The freestream conditions correspond to those of the experimental work of Monnerie and Werle[9], the specifics of which are given in the table on Figure 1. A comparison of pitot pressure contours from reference 8 to the current $\alpha = 10°$ solution is given in Figure 4. Both solutions are a marked improvement over the results of reference 7 which employed a conical approximation and did not capture the secondary separation. However, while the shape and location of the primary and secondary vortices are roughly the same, the pitot pressure levels on the wing upper surface are not. The solution of reference 8 shows less evidence of pitot pressure loss in the primary vortex region as shown by the large disparity in the $P_T/P_{T\infty} = 0.7$ pressure levels. This may be attributed to the improved resolution in the leading-edge tip region which leads to a more accurate computation of the leading-edge expansion, hence the improved correlation with experiment as shown in Figure 5. The expanded grid size in the η and ζ-directions may also account for some of this improvement as the outer boundaries are much farther from the wing. In addition, the increased resolution of the apex region by the addition of the $\frac{X}{L} = 0.05$ station improves the modeling of the flow being entrained into the inviscid core.

The improved resolution in the η or y direction accounts for the increased clarity of the upper surface "oil flow" patterns shown in Figure 6. While the position of the primary and secondary lines of separation (S_1 and S_2 respectively) and reattachment (A_1, A_2) are nearly the same, their sharpness, particularly near the trailing edge, is improved. This improvement is attributed to a second-order treatment of the downstream boundary condition. However, in spite of these differences, the aerodynamic loading perceived on the wing is similar as shown in the C_p distributions given in Figure 7. Here the suction peaks associated with the primary and secondary vortices are clearly in evidence and are similarly located.

The development of the cross-plane velocity with X is illustrated in Figures 8 and 9 for 10° and 20° respectively. Here the growth of the primary and secondary vortices and their inboard migration with angle of attack are evident and the non-conical nature of the flow field near the apex is revealed. Interesting to note is the fact that the secondary vortex originates at approximately $\dfrac{X}{L} = 0.3$ for both cases. These same features are also evident in the upper surface "oil flow" pattern given in Figure 10. While the flow is non-conical in the apex region, analysis of Figures 7-10 indicates that for the majority of the planform the flow is fairly conical.

The effect of angle of attack on loading is emphasized in the comparison of pressure coefficient depicted in Figure 11. The expected increase in loading and the inboard shift of vortex-associated surface pressure loss with α is evident. From analysis of the pitot pressure contours in Figure 12 one can observe the growth of the secondary vortex and its displacement effect on the primary. The increased circumferential velocity in the primary vortex with angle of attack induces the observed pressure loss in the vortex core. Comparison of the 20° solution to the experiment of Monnerie and Werle in Figure 13 illustrates the remarkable accuracy of the laminar Navier-Stokes computation in spite of the rather high Reynolds number of the experiment.

CONCLUSIONS AND DISCUSSIONS

Steady laminar solutions of the full 3-dimensional Navier-Stokes equations have been generated for the supersonic (M = 1.95) flow over a 75° sweep sharp-edged delta wing at 10° and 20° angles of attack. Comparison with experiment and with the Navier-Stokes solution of reference 8 shows the following:

1. For both cases, the flow field solution correlates well with experiment. The position and strength of the primary and secondary vortices are accurately predicted. This leads one to believe that a laminar Navier-Stokes solution to the leading-edge vortex problem is adequate for obtaining pitot pressure, particularly for configurations with a Reynolds number less than 1 x 10^6 such as in the present study, at least until an adequate turbulence model is developed for vortical flows.

2. An accurate geometrical modeling of the leading edge and considerable resolution of the tip region appear critical to the accurate computation of the leading-edge expansion. The agreement obtained in the present study is attributed in part to these two modifications to the grid of reference 8. A more accurate treatment of the downstream boundary condition also accounts for the improved solution in the trailing-edge region. In addition, the expansion of the computational domain in the η and ζ directions probably resulted in some improvement in the 10° solution.

3. Because secondary separation develops axially as well as radially, methods employing a conical assumption will not adequately resolve a large portion of the flow field. In addition, resolution of the apex region is critical due to its highly non-conical structure.

4. The use of a local timestepping procedure increased the convergence rate by roughly a factor of two. It is estimated that each solution of the laminar 3-dimensional compressible Navier-Stokes equations presented herein required approximately 2 hours of CPU time on a CRAY 1-S computer to reach steady state based on a four order of magnitude reduction in L2NORM for all dependent variables.

REFERENCES

1. Weber, J.A., Brune, G.W., Johnson, F.T., Lu, P., and Rubbert, P.E., "Three-Dimensional Solution of Flows over Wings with Leading-Edge Vortex Separation," AIAA Journal, Vol. 14, April 1976, pp 519-525.

2. Luckring, J.M., Schoonover, W.E., Jr., and Frink, N.T., "Recent Advances in Applying Free Vortex Sheet Theory for the Estimation of Vortex Flow Aerodynamics," AIAA Paper 82-0095, Jan. 1982.

3. Hoeijmakers, H.W.M., and Rizzi A., "Vortex Fitted Potential Solution Compared with Vortex-Captured Euler Solution for Delta Wing with Leading-Edge Vortex Separation," AIAA Paper 84-2144, 1984.

4. Erikson, L.E., and Rizzi, A., "Computation of Vortex Flow Around Wings Using the Euler Equations," Proceedings of the Fourth GAMM Conference on Numerical Methods in Fluid Mechanics, Notes on Numerical Fluid Mechanics, Vol. 5, 1981, pp 137-148.

5. Hitzel, S.M., and Schmidt, W., "Slender Wings with Leading-Edge Vortex Separation - A Challenge for Panel-Methods and Euler-Codes," AIAA Paper 83-0562, Jan. 1983.

6. Newsome, R.W., "A Comparison of Euler and Navier-Stokes Solutions For Supersonic Flow Over a Conical Delta Wing," AIAA Paper 85-0111, January 14-17, 1985.

7. Vigneron, Y.C., Rakich, J.V., and Tannehill, J.C., "Calculation of Supersonic Viscous Flow over Delta Wings with Sharp Subsonic Leading Edges," AIAA Paper 78-1137, July 1978.

8. Rizzetta, D.P., and Shang, J.S., "Numerical Simulation of Leading-Edge Vortex Flows," AIAA Paper No. 84-1544, July 1984.

9. Monnerie, B., and Werle, H., "Study of Supersonic and Hypersonic Flow About a Slender Wing at an Angle of Attack," AGARD CP-30, May 1968 (in French).

10. MacCormack, R.W., "The Effect of Viscosity in Hypervelocity Impact Cratering," AIAA Paper 69-354, Apr-May 1969.

11. MacCormack, R.W., and Baldwin, B.S., "A Numerical Method for Solving the Navier-Stokes Equations with Application to Shock-Boundary Layer Interactions," AIAA Paper 75-1, Jan. 1975.

12. Shang, J.S., Buning, P.G., Hankey, W.L., and Wirth, M.C., "Performance of a Vectorized Three-Dimensional Navier-Stokes Code on a CRAY-1 Computer," AIAA Journal, Vol. 18, Sep. 1980, pp 1073-1079.

TABLE I COMPUTATIONAL PARAMETERS

M	α	Δ	y_{min}/z_{LE}	y_{max}/z_{LE}	z_{max}/z_{LE}	Iteration
1.95	10°*	9.7971×10^{-1}	−3.0	3.25	2.75	6000
1.95	10°	7.973×10^{-1}	−3.7	4.6	3.5	2500
1.95	20°	7.973×10^{-1}	−3.7	4.6	3.5	2500

* Reference 8
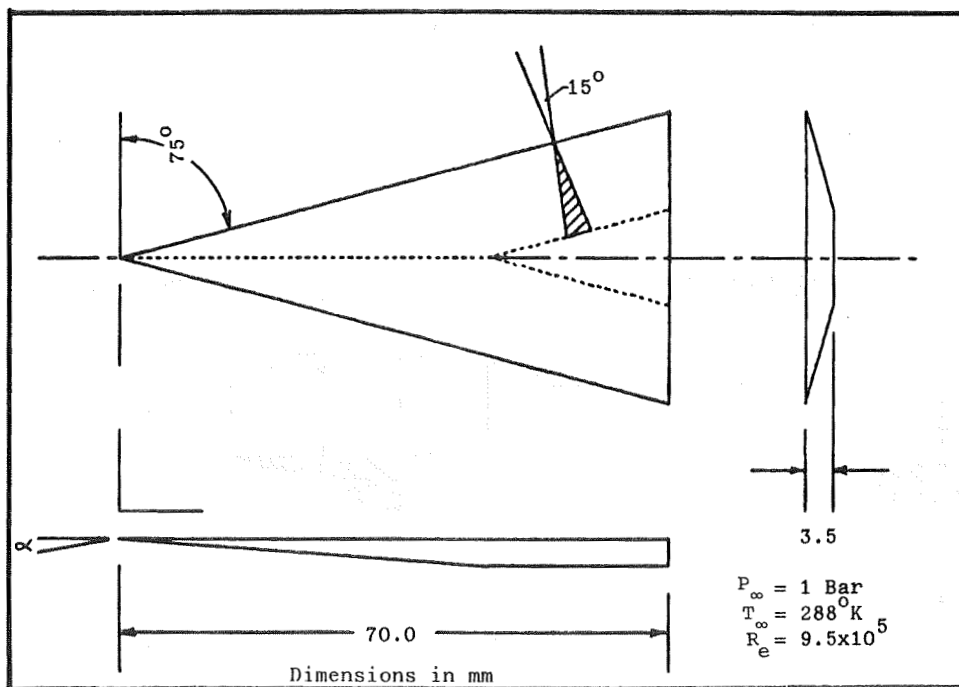
Figure 1. Delta wing geometry.
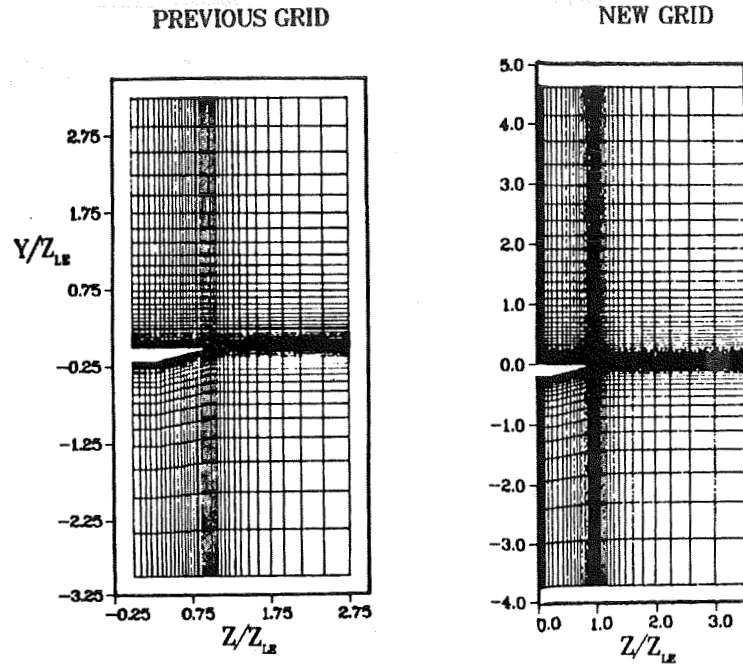
Figure 2. Comparison of Y-Z grid structure.
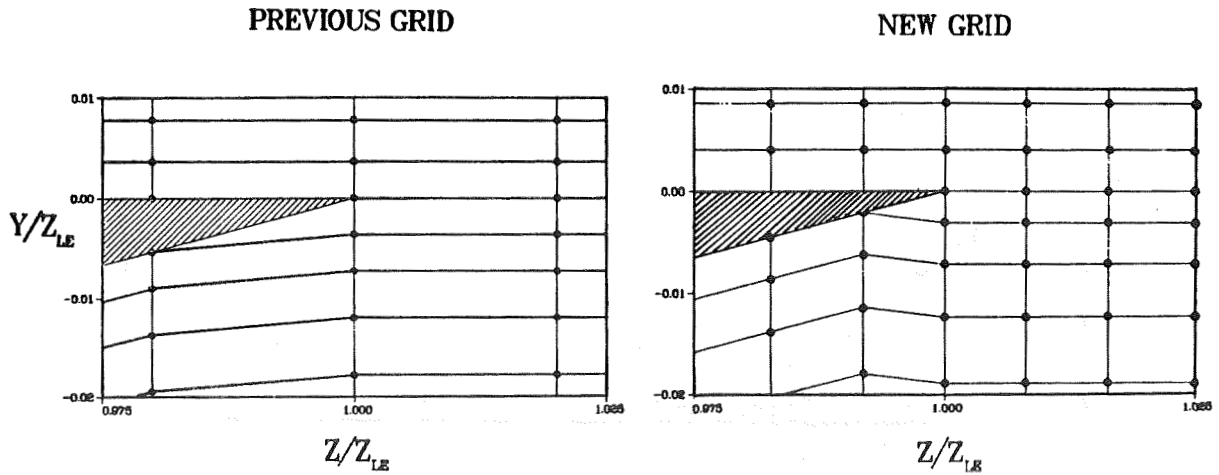
Figure 3. Comparison of Y-Z grid structure in tip region.
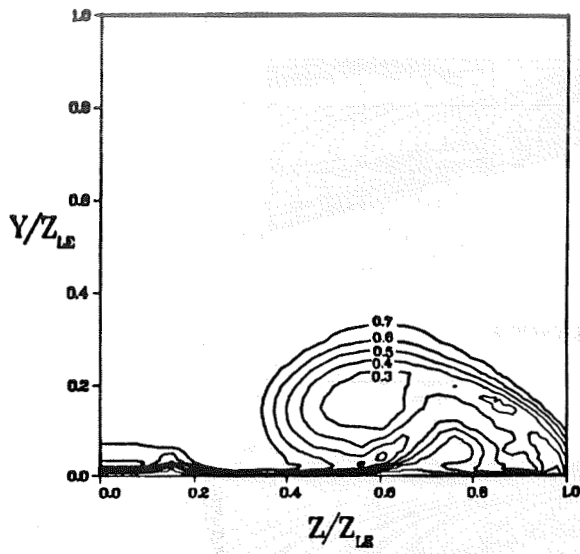
REFERENCE 8   PRESENT STUDY
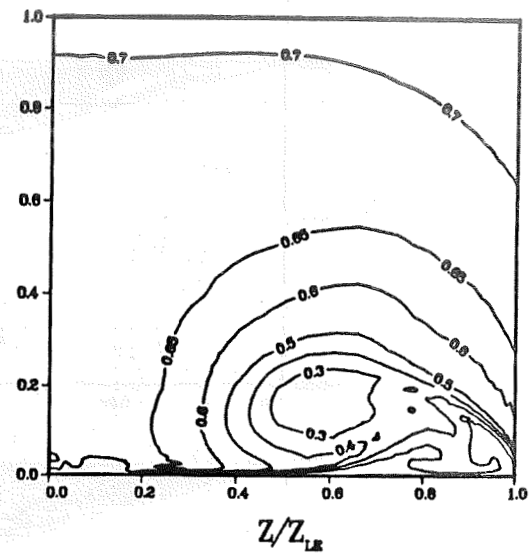
Figure 4. Comparison of Pitot pressure, X/L = 0.8.

EXPERIMENT   PRESENT STUDY
REFERENCE 9
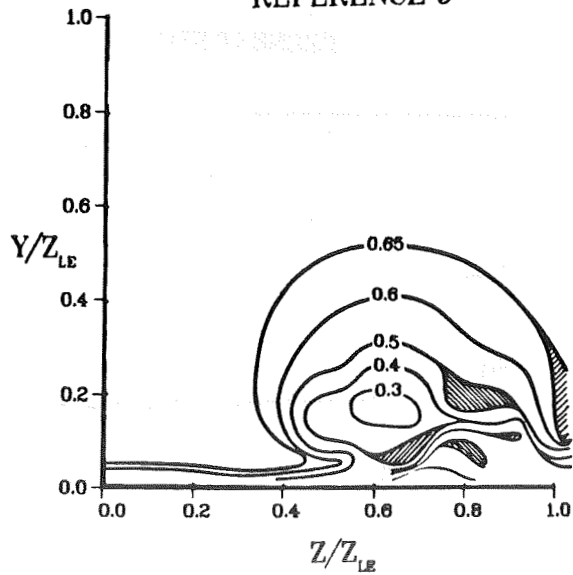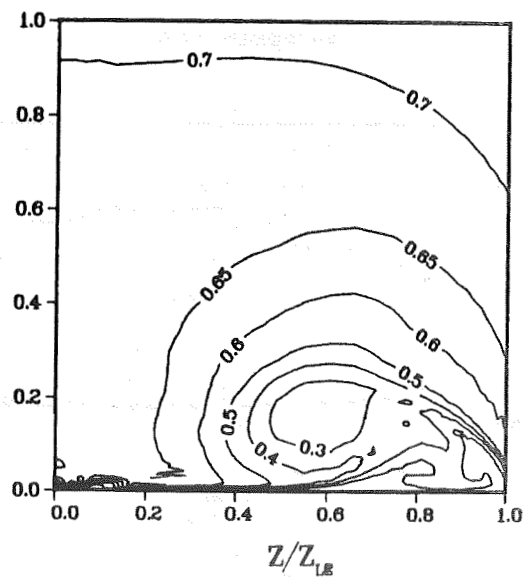
Figure 5. Comparison of Pitot pressure, X/L = 0.8.
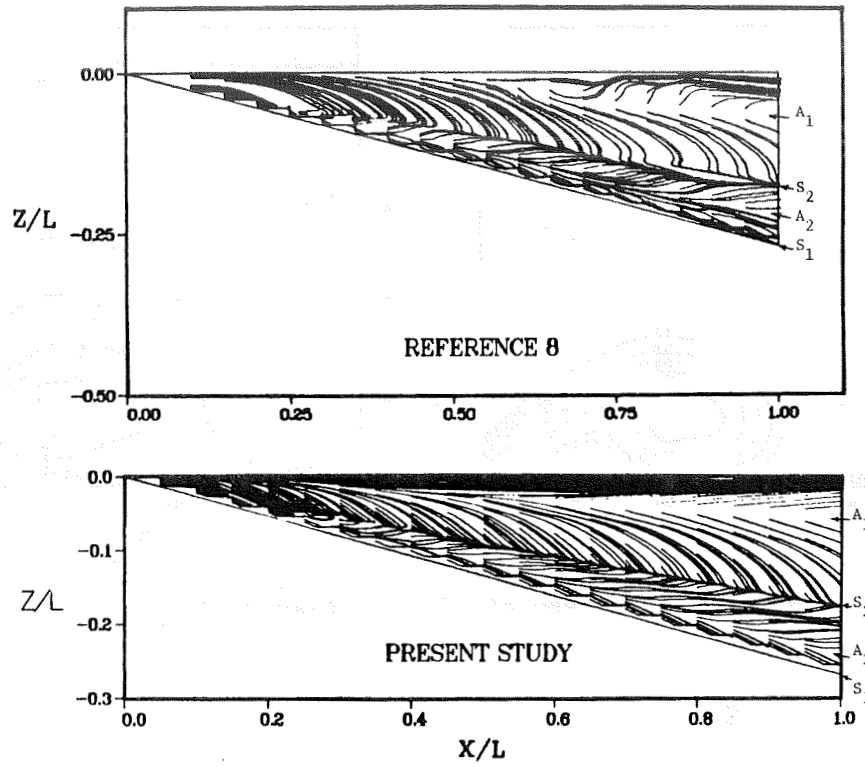
Figure 6. Upper surface oil flow pattern, $\alpha = 10°$.
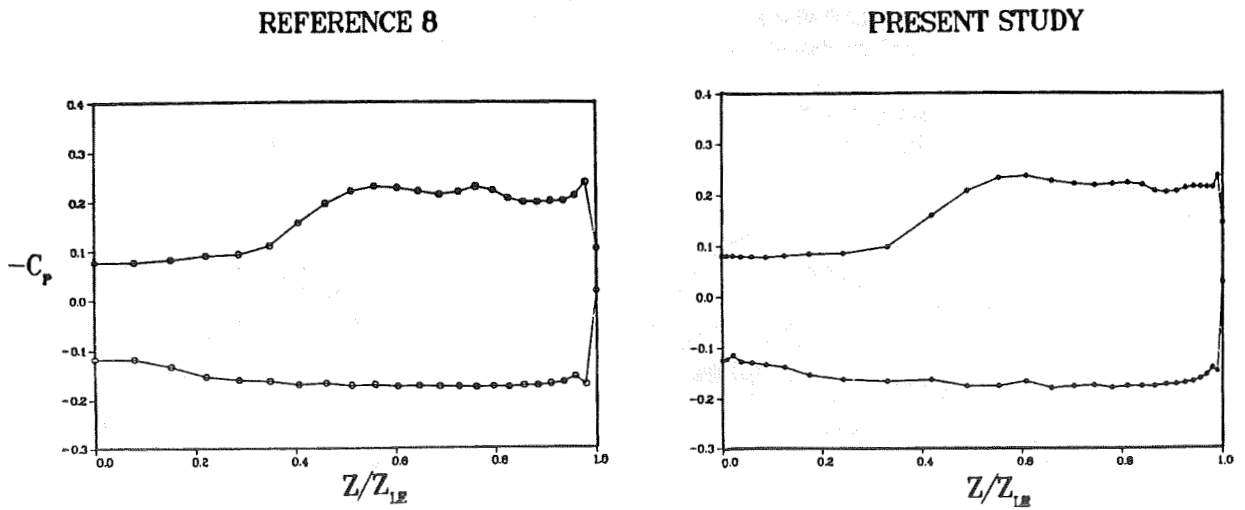

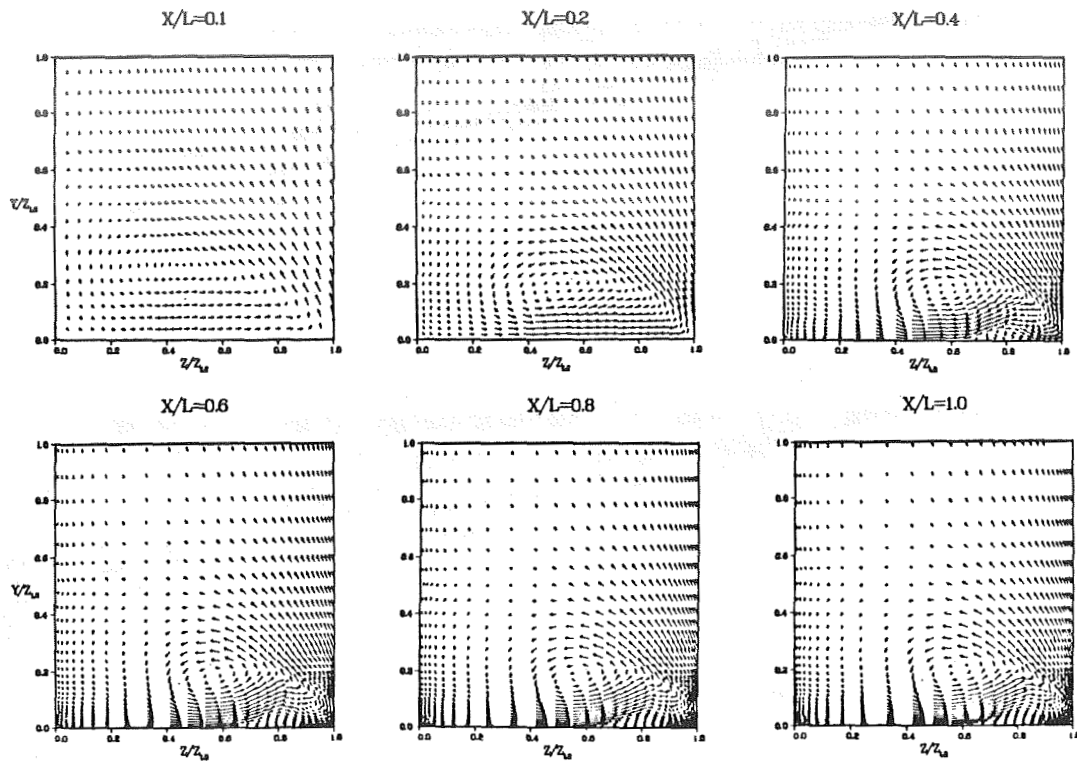Figure 7. Spanwise pressure distribution, $\alpha = 10°$ $X/L = 0.8$.

X/L=0.1   X/L=0.2   X/L=0.4

X/L=0.6   X/L=0.8   X/L=1.0

Figure 8. Development of cross-plane velocity, $\alpha = 10°$.

X/L=0.1   X/L=0.2   X/L=0.4

X/L=0.6   X/L=0.8   X/L=1.0
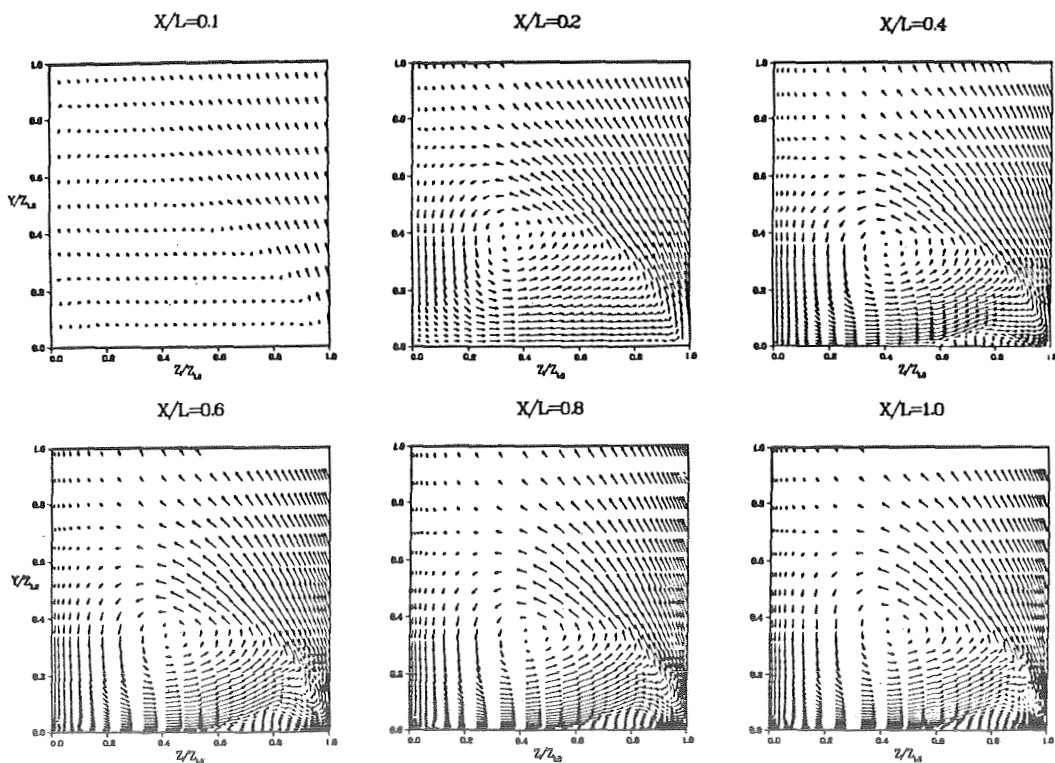
Figure 9. Development of cross-plane velocity, $\alpha = 20°$.
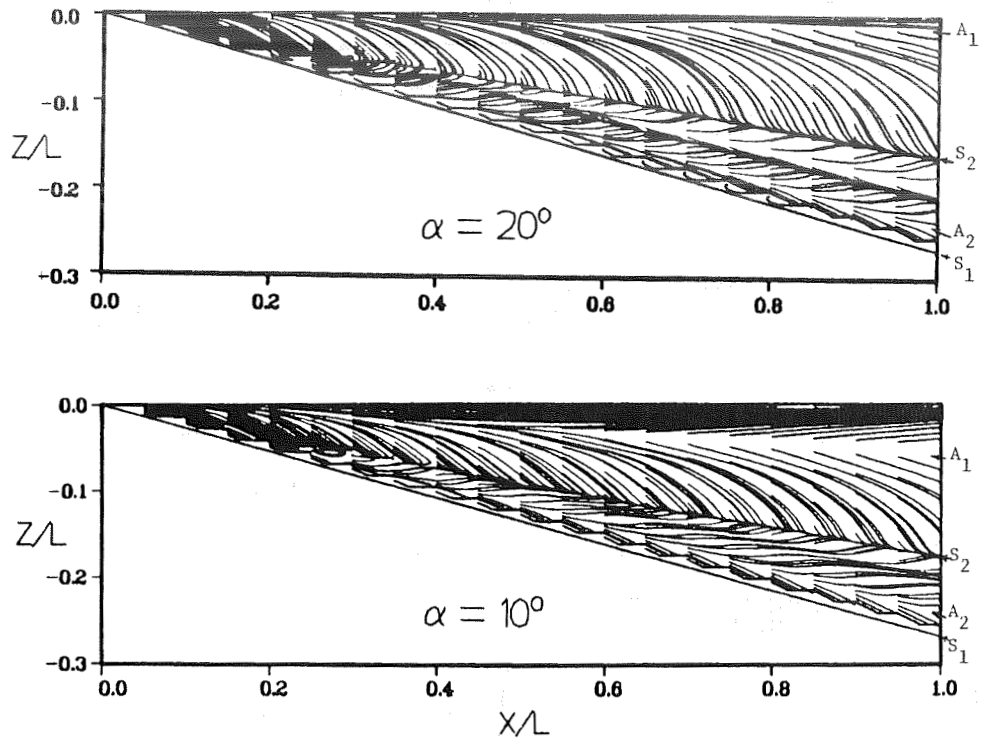
Figure 10. Upper surface oil flow pattern.
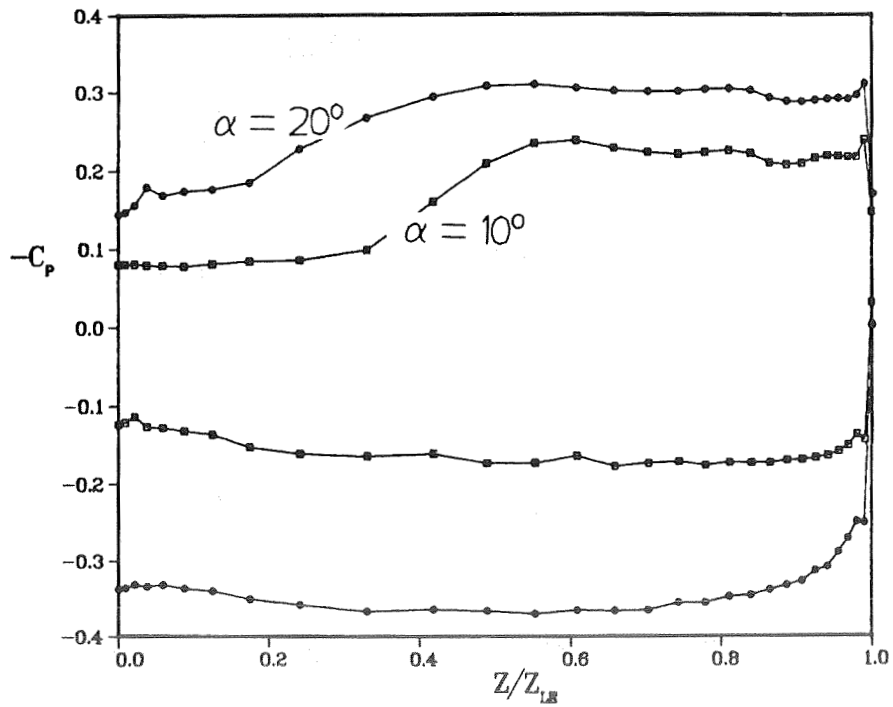
Figure 11. Effect of α on pressure distribution, $X/L = 0.8$.

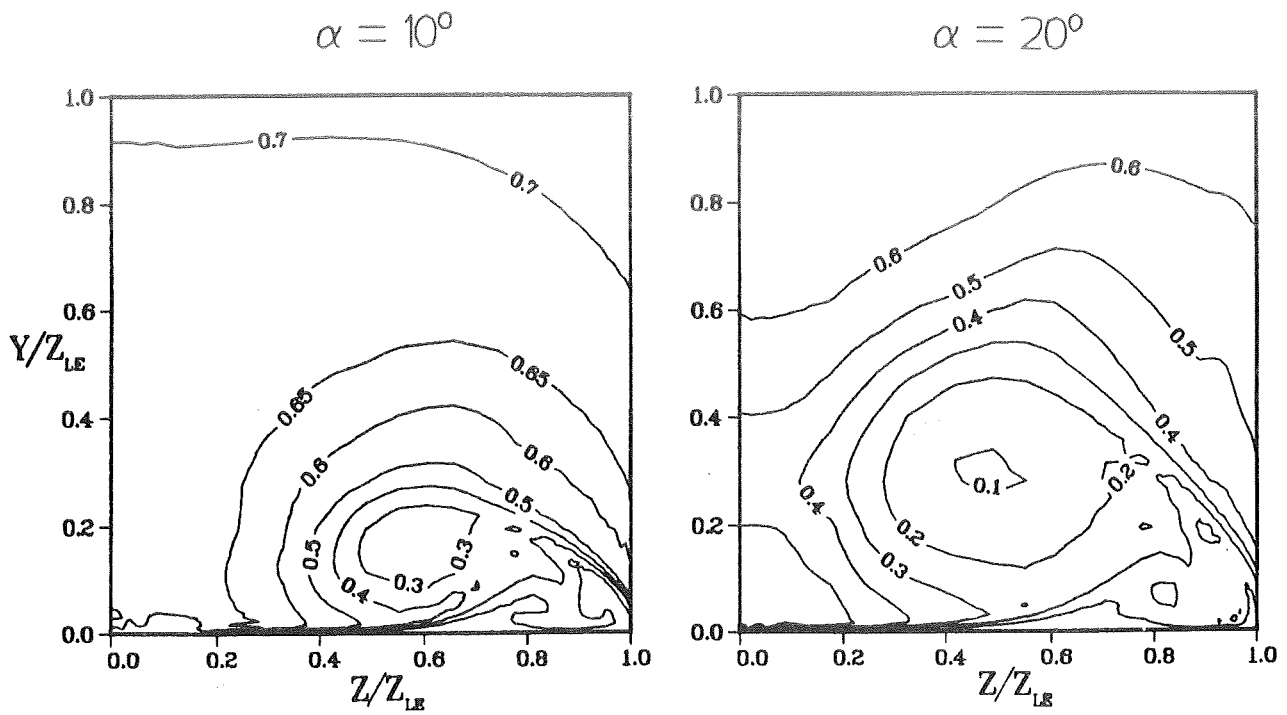$\alpha = 10°$ $\alpha = 20°$

Figure 12. Effect of α on Pitot pressure, $X/L = 0.8$.

REFERENCE 9
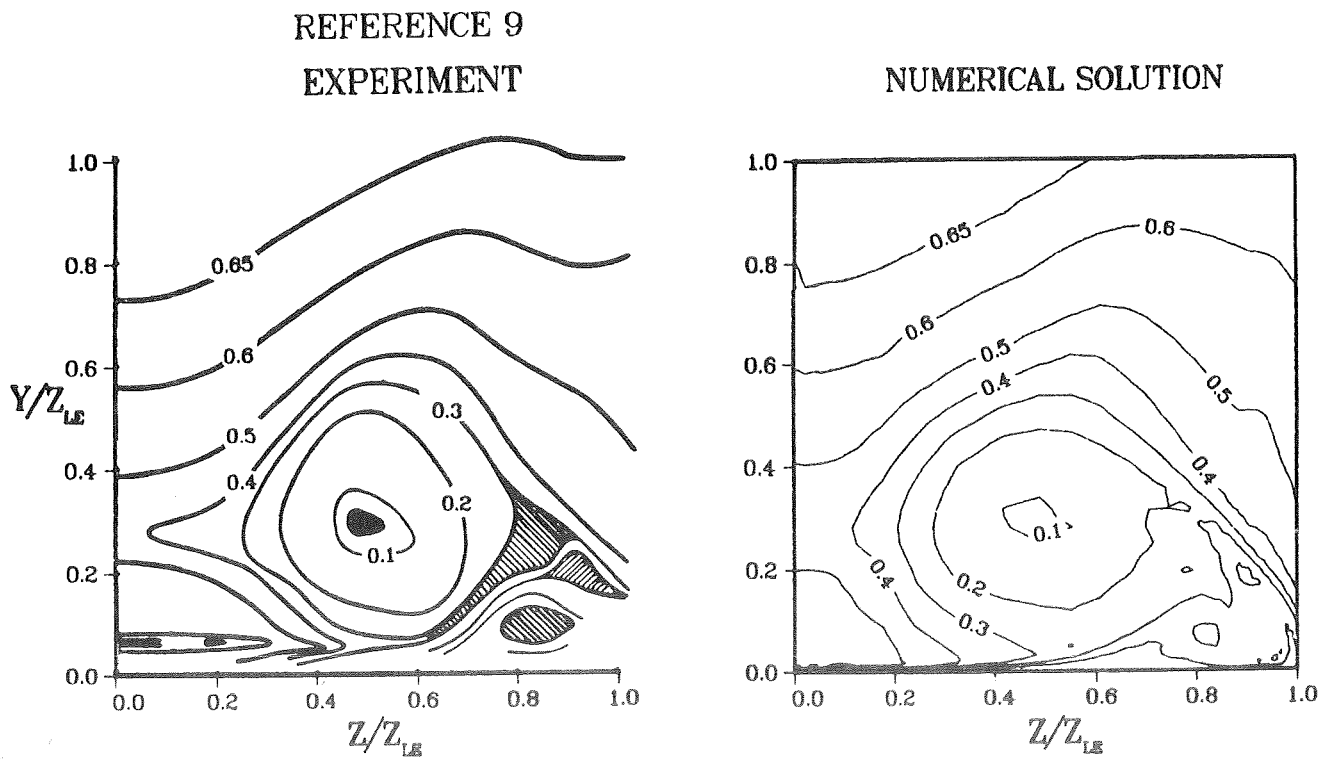EXPERIMENT   NUMERICAL SOLUTION

Figure 13. Comparison of Pitot pressure, $\alpha = 20°$.